metals

MDPI

Article

A New S-Shape Specimen for Studying the Dynamic Shear Behavior of Metals

Ali Arab *, Yansong Guo, Qiang Zhou * and Pengwan Chen *

State Key Laboratory of Explosion Science and Technology, Beijing Institute of Technology, Beijing 100081, China
* Correspondence: arabali83@yahoo.com (A.A.); zqpcgm@gmail.com (Q.Z.); pwchen@bit.edu.cn (P.C.); Tel.: +86-156-0125-4524 (A.A.); +86-6891-8740 (P.C.)

Received: 8 July 2019; Accepted: 27 July 2019; Published: 29 July 2019

Abstract: A new S-shaped specimen geometry is developed in this study to investigate the shear behavior of materials under dynamic shear condition. Traditionally, hat-shaped geometry is used to study the dynamic shear of materials by a conventional split Hopkinson pressure bar apparatus. However, in this geometry, the force equilibrium on the two sides of the sample is difficult to fulfill, and the stress field in the shear region is not homogeneous. Hence, the calculated shear stress–strain curve from this geometry is not precise. To overcome this problem, the new S-shaped specimen is designed to achieve accurate shear stress–strain curve. This geometry can be used in a wide range of strain rates and does not require additional machining process for microstructure observation. The new S-shaped specimen is successfully coupled with digital image correlation method because of the flat surface. Digital image correlation results indicate that the fracture patterns of the new S-shaped specimen occur with maximum shear strains in the shear region in the middle of the sample. This result is also validated by finite element model simulation. The new S-shaped specimen geometry can be used to study the dynamic shear behavior of various metals.

Keywords: dynamic shear behavior; adiabatic shear banding; split Hopkinson pressure bar; high strain rate; titanium

1. Introduction

Regardless of loading condition, plastic deformation of ductile materials occurs in shear [1]. Under high strain rate conditions, deformation of the ductile materials is often associated with shear banding instead of cracking. Adiabatic shear banding (ASB) is a catastrophic failure mechanism in which large deformations occur in a narrow area (approximately 5–100 μm) [2]. The local temperature in this narrow band may reach a significant fraction of the melting temperature, which may lead to recrystallization [3]. ASB occurs in many applications, such as ballistic impact, machining process, forging, and penetration. Many experimental and analytic studies have been conducted on the formation of ASB [4–8]. However, testing the materials under dynamic shear condition is not straightforward.

Various types of test techniques and sample geometries were designed to investigate materials under dynamic shear condition. Different test apparatuses, such as split Hopkinson bar [9], gas gun [10], drop-weight test [11], and uniaxial hydraulic apparatus have been used for this purpose. Meanwhile, different geometries, such as torsional sample [12], sheet sample [1], flat or cylindrical hat-shaped sample [13,14], shear compression specimen [15–17], double shear sample [18], compact forced simple shear sample [19], and single- or double-edged sample [11] were used in these techniques. Among these specimens, shear deformation is constrained in specific sections because of their geometrical discontinuities. A hat-shaped specimen is one of the geometries that are mostly utilized in shear experiments because of its simple geometry [20–22]. In this geometry, the stress and strain states are not homogeneous at the shear region [23]. Moreover, the two sides of the sample do not achieve

force equilibrium [11]. Thus, the calculated shear stress–strain from this geometry is a rough estimate and inaccurate [19,23]. In addition, the shearing region rotates during testing due to the overlapping nature of the shear area in this geometry. To overcome these problems, Ran et al. [24] adopted the flat hat-shaped sample combined with digital image correlation (DIC) measurement. They measured force and punching displacement from the split Hopkinson pressure bar (SHPB) and shear strain by the DIC method. They achieved accurate strain rate and also calculated the shear engineering stress and strain using the DIC method. However, without using the DIC method, obtaining the shear stress–strain curve is impossible using this geometry. Rittel et al. [3] developed a new geometry for shear test. In this sample, by applying compressive loading a shear dominant field occurs in the gauge section. This geometry can be used in static and dynamic loadings, as well as in different temperatures. However, this sample design does not constitute a 'simple' shear loading stress state within the gauge section but a rather three-dimensional stress state. Moreover, this geometry leads to a radial inertial effect of the sample motion under dynamic loading [19]. Recently, Xu et al. [11] proposed a new double side sample to study the shear band. They observed good agreement between the experimental and simulation results in a wide range of strain rates. However, they designed a special sample fixture to ensure that the shear would be symmetrical. They also used an aluminium bar as the transmitted bar because of the weak transferred pulse. Gray et al. [19] also designed a compact forced simple shear sample to study shear localization in materials. Although this sample could produce pure simple shear, it has a complicated design and required difficult machining process.

In the present study, a new S-shaped sample (NSSS) is proposed for the dynamic shear test through the conventional SHPB. This paper is divided into two parts. In the first part, the detail of the new sample and experimental setup are shown and discussed. In addition, DIC method is used to study the shear strain field in the sample. In the second part, the results of the experiments and the DIC method are compared via numerical simulation. The results of the experiments and simulation show good agreement in a wide range of strain rates.

2. Materials and Methods

2.1. Materials and Specimens

The NSSS design is schematically shown in Figure 1. It is designed to achieve the pure shear stress field parallel to the loading direction in the shear zone (the middle part of the specimen). The thickness of the middle part (t_m) is selected as 1, 1.5, 2, and 2.5 mm to generate different shear strain rates. The width of shear zone (W_s) for all specimens is kept constant (0.2 mm). This value is selected by the trial and error. The length of the shear zone (L_s) can easily be calculated by Equation (1). Samples are fabricated by the wire cutting technique from the Ti6Al4V titanium alloy.

$$L_s = \sqrt{{t_m}^2 + {W_s}^2} \tag{1}$$

The conventional SHPB is used to apply dynamic loading in this paper. The NSSS is sandwiched between the incident and transmitted bars. The contact surfaces of the bars and sample are sufficiently lubricated by Vaseline to reduce friction and specimen barrelling. The lengths of the striker, incident bar, and transmitted bar are 300, 1200, and 1200 mm, respectively. All the bars have the same diameter (14 mm) and are made of hardening 18% nickel maraging steel. The two strain gauges are mounted in the middle of the incident and transmitted bars to capture the stress wave. The other strain gauge is installed on the incident bar to be used as a trigger of the high-speed camera. The schematic setup of the SHPB is shown in Figure 2.

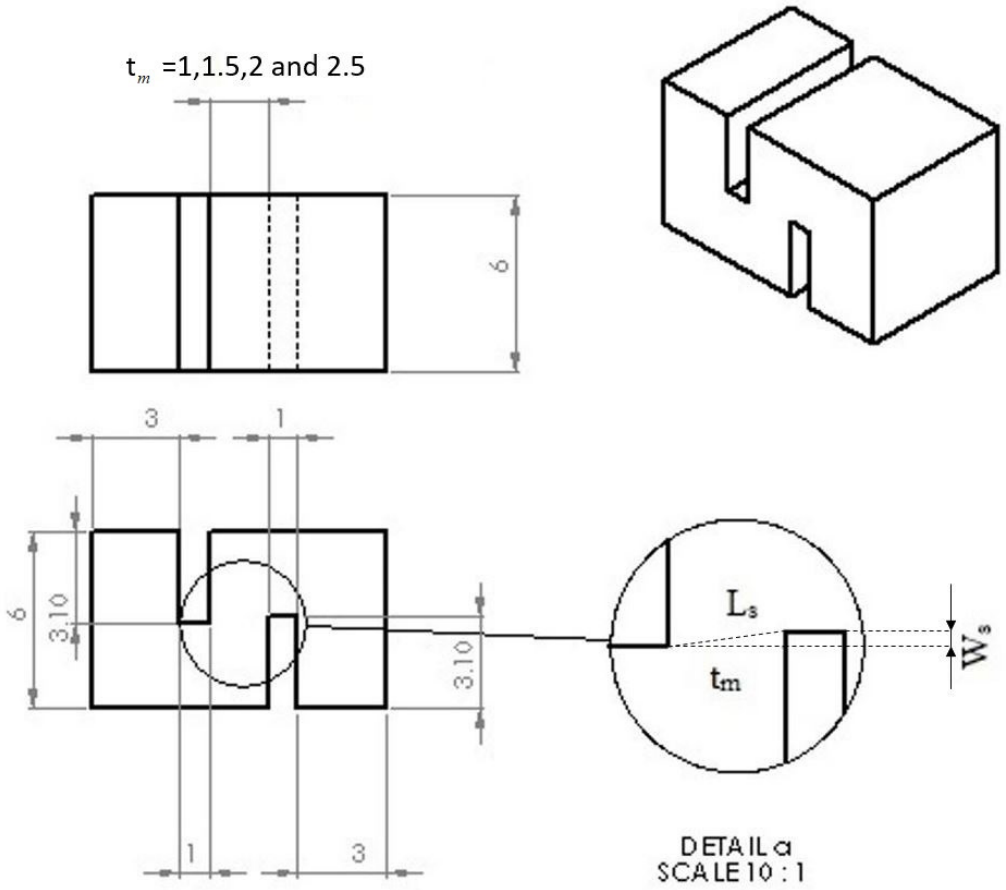

Figure 1. Schematic design of the new S-shaped sample (NSSS).

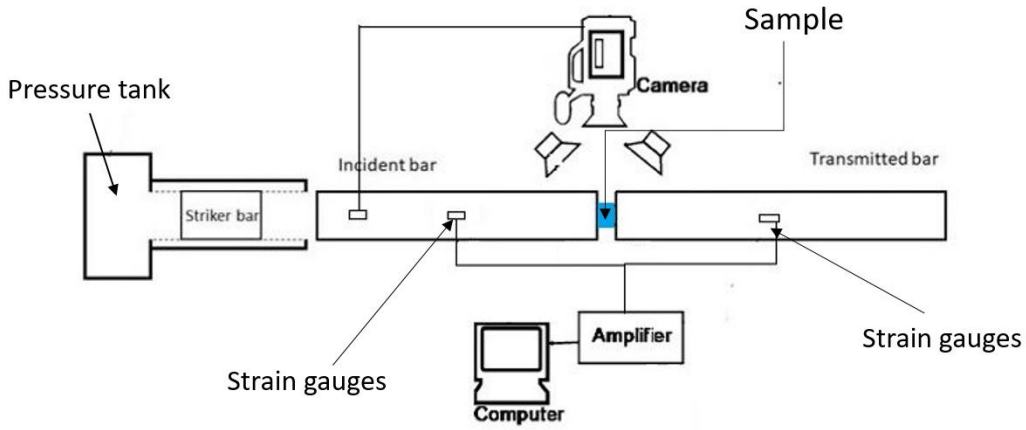

Figure 2. Schematic set up of the experiment.

Assume that the stress waves propagate in the incident and transmission bars without dispersion. The load and displacement of the sample can be determined

$$F_{in} = A_b E(\varepsilon_i(t) + \varepsilon_r(t)), \tag{2}$$

$$F_{out} = A_b E\varepsilon_t(t), \tag{3}$$

$$F_{ave} = \frac{(F_{in} + F_{out})}{2}, \tag{4}$$

$$U_{in} = C\int_0^t (\varepsilon_i(t) - \varepsilon_t(t))dt, \tag{5}$$

$$U_{out} = C\int_0^t \varepsilon_t(t)dt, \tag{6}$$

$$U_{rel} = U_{in} - U_{out}, \tag{7}$$

where F_{in} is the force on the sample surface in contact with the incident bar; F_{out} is the force on the sample surface in contact with the transmitted bar; U_{in} and U_{out} are the displacements of the surfaces of the incident and transmitted bars, respectively; ε_i, ε_t and ε_r are the incident, transmitted, and reflected strains, respectively; A_b, E, and C are the bar area, Young's modulus and wave velocity of the bars, respectively; F_{ave} is the average force in the sample; and U_{rel} is the relative displacement. Shear stress τ, shear strain γ, and shear strain rate $\dot{\gamma}$ in the specimen are calculated as follows:

$$\tau(t) = \frac{F_{ave}}{A_s}, \tag{8}$$

$$\gamma(t) = \frac{U_{rel}}{L_S}, \tag{9}$$

$$\dot{\gamma}(t) = \frac{C_1(\dot{\varepsilon_i(t)} - \varepsilon_r(t) - \varepsilon_t(t))}{L_S}, \tag{10}$$

where L_s is the length of the shear zone, which is calculated using Equation (1).

2.2. DIC Measurement

The DIC method is used to investigate the strain field of the sample. From the SHPB wave signal analysis, only the average amount of shear stress and strain of the sample can be calculated. With DIC, determining the full-field strain distribution of the sample is possible. However, this method is not a standardized technique and its accuracy depends on many factors. DIC is a non-contact optical method and provides a full-field measurement of deformation in the specimen. In literatures, the basic principle of the DIC method was fully described [25,26]. A comprehensive information of the distribution of strain over the NSSS is obtained by this method, in which a random pattern of speckles is applied to the specimen surface. The speckled pattern is applied by coating the surface of the NSSS with a layer of white paint using a spray can. The black speckles are then applied by lightly over-spraying a black mist of paint. Figure 3 shows the surface of the sample with speckles. A high-speed digital camera is used to record the consecutive changes of the speckled pattern when the NSSS is subjected to high strain rate loading. The camera is triggered by electrical signals that are provided by the strain gauge mounted on the incident bar 50 cm from the impact face. The camera frame rate is set at 150,000 fps. A spatial resolution of 256 × 144 pixels can sufficiently monitor an area of 10 × 6 mm of the NSSS surface.

The displacement strain field of the NSSS during the SHPB experiments is analyzed using commercial VIC-2D (Version 2009.1.0, Correlated Solutions Incorporated, 120 Kaminer Way Parkway Suite, Columbia, SC, USA) technique. The images are processed using a 12 × 12 pixel subset, step size 1, and spline cubic interpolation.

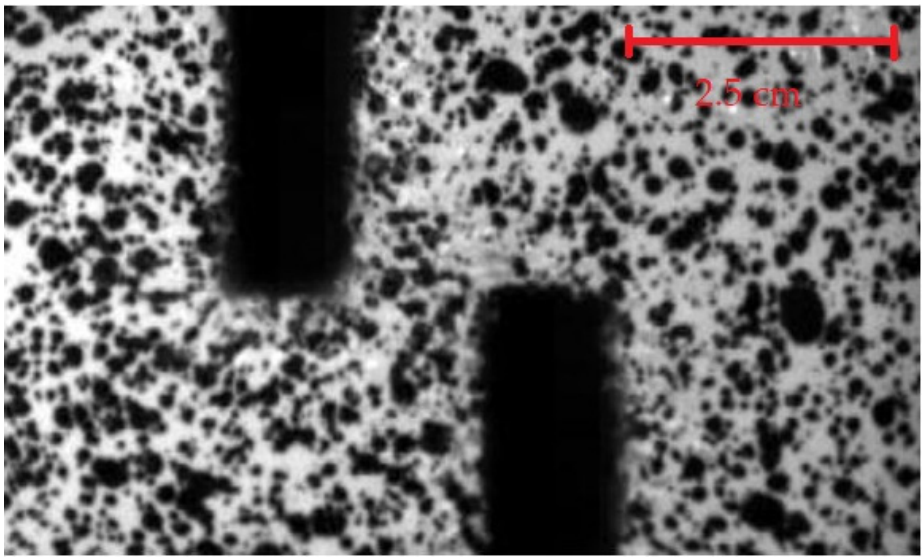

Figure 3. NSSS with a random speckled pattern.

2.3. Finite Element Model (FEM) and Material Parameters

ABAQUS Explicit (Version 6.9-3; Dassault Systemes Simulia Corp: Providence, RI, USA, 2010) is used in simulating the operation process of dynamic tests using SHPB to verify the applicability and availability of the NSSS. The explicit FEM of the entire structure is established, including the striker bar, incident bar, specimen, and transmitted bar.

The Johnson–Cook (J–C) material model is used for the plastic deformation of the NSSS. The J–C model is an outstanding and widely used model for the simulation of dynamic loading conditions, which introduce the strain hardening, strain rate, and thermal softening effects of the materials. The failure parameter is not considered in this study. The J–C constitutive model is usually expressed as [27]

$$\overline{\sigma} = (A + B\overline{\varepsilon}^{n})\left[1 + C\ln\left(\frac{\dot{\overline{\varepsilon}}}{\dot{\overline{\varepsilon_0}}}\right)\right]\left[1 - \left(\frac{T - T_{room}}{T_m - T_{room}}\right)^{m}\right] \quad (11)$$

where $\overline{\sigma}$ is the equivalent plastic flow stress, $\overline{\varepsilon}$ is the equivalent plastic strain, $\dot{\overline{\varepsilon}}$ is the equivalent plastic strain rate, $\dot{\overline{\varepsilon_0}}$ is the reference equivalent plastic strain rate, T is the absolute temperature, T_{room} denotes the reference room temperature, T_m is the melting temperature of the materials, and A, B, n, C, and m describe the degree of plastic deformation of the materials, in which A, B, and n are the coefficients of material strain hardening, C is the coefficient of strain rate hardening, and m is the thermal softening coefficient of materials.

Table 1 lists the material properties of the samples and bars used in the model. Table 2 shows the parameters J–C model for the Ti6Al4V.

Table 1. Material properties used in FEA, data from [28].

Part	Material	Density, kg/m^3	Elastic Modulus, E (GPa)	Poisson's Ratio	Specific Heat, Cp (J/kg °C)	T_{melt}, (K)	T_{room} (K)
Specimen	Ti-6Al-4V	4300	110	0.33	670	1903	298
Bar	Steel	7800	190	0.33	–	–	–

Table 2. J–C constitutive model parameters of Ti-6Al-4V, data from [28].

Set	A (MPa)	B (MPa)	N	C	m	$\overline{\varepsilon_0}$ (s^{-1})
J–C	862	331	0.34	0.012	0.8	1

Figure 4 shows the numerical simulation model. The sample is initially sandwiched between the incident and transmitted bars. An eight-node linear brick, reduced integration, and coupled displacement-temperature element (C3D8RT) is selected for the bars and specimen. The size of the applied load velocity for each test condition is obtained based on the actual loaded stress wave analysis to ensure the simulation reliability of the results. The wave velocity in the steel bar is 5000 m/s, and the length of the bar is 1.2 m. Therefore, the terminal time of calculation is set to 500 µs to ensure that the specimen undergoes a complete primary stress wave loading (three phases of incident, reflected and transmitted). The length of the analysis step is adjusted according to the test conditions.

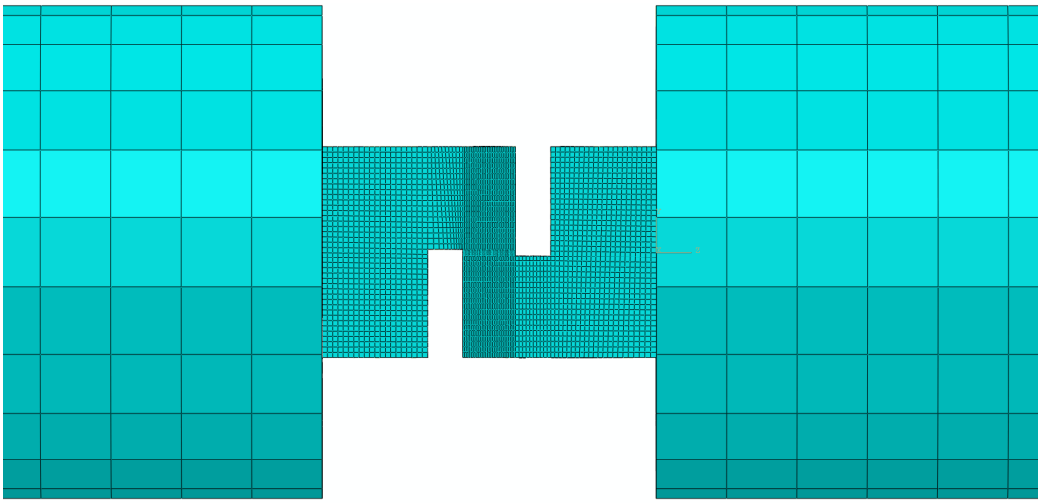

Figure 4. FEM meshes for the NSSS.

3. Results and Discussion

3.1. Dynamic Test (SHPB)

The samples were tested using SHPB at different strain rates. Before finalizing the geometry of the NSSS, different geometries were tested. The bending was observed for the sample with a middle dimension of 2.5 mm. To avoid complex stress field in the middle part of the specimen, the t_m was limited to 2 mm. Figure 5 shows the strain wave signals captured on the bars of SHPB (for comparison, all the signals were shifted at the same starting point) for the sample with t_m = 1.5 and a shear strain rate of 2800 s^{-1}. Transmitted strain (ε_t) shows that after the steady state the strain drops and fracture occurs. The duration of the transmitted strain is shorter than the incident pulse, showing that the fracture occurs under the first stress wave. However, increasing the velocity of the striker bar to achieve a higher strain rate weakened the signal in the transmitted bar; to overcome this problem, the transmitted bar could be changed into an aluminium bar or a semiconductor strain gauge could be used [29].

Equations (2) and (3) indicate that the forces applied to the two sides of the samples are determined from the captured strain signals. Figure 6 shows the calculated F_{in}, F_{out}, and F_{ave} for the sample with t_m = 1.5 mm. During the rising time, the F_{out} is higher than F_{in}, and after 30 µs, the forces in both sides are equal. However, the force values of F_{in} and F_{out} at the plateau stage are close, and the calculated average value of the force (F_{ave}) nearly overlaps with them. This result indicates that the force equilibrium condition was reached. The force equilibrium is checked for all the specimens with different t_m, and in all of them, the force equilibrium conditions were achieved.

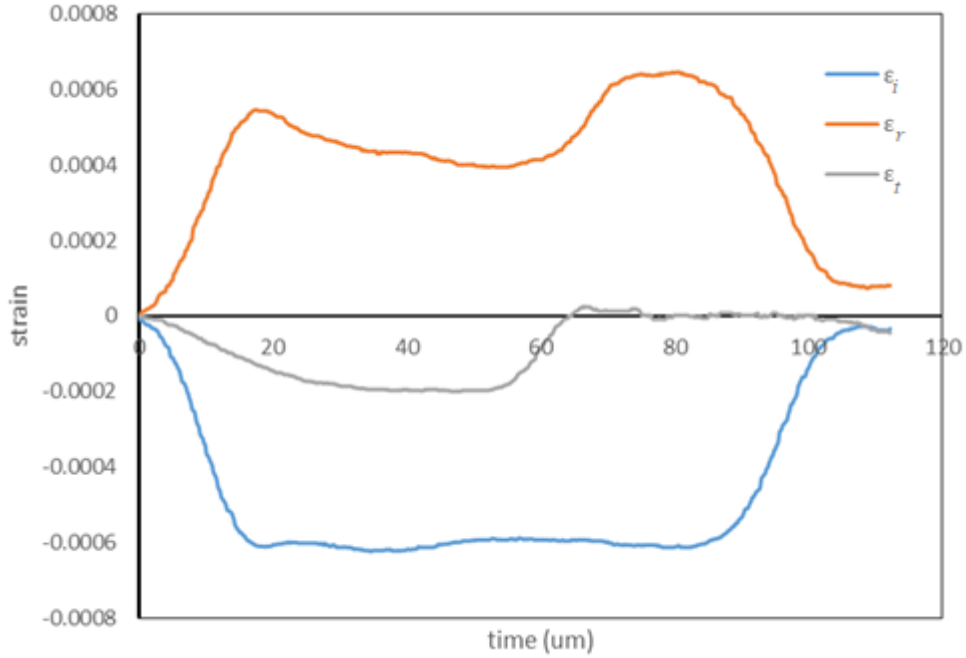

Figure 5. Split Hopkinson pressure bar (SHPB) wave signal for the NSSS sample.

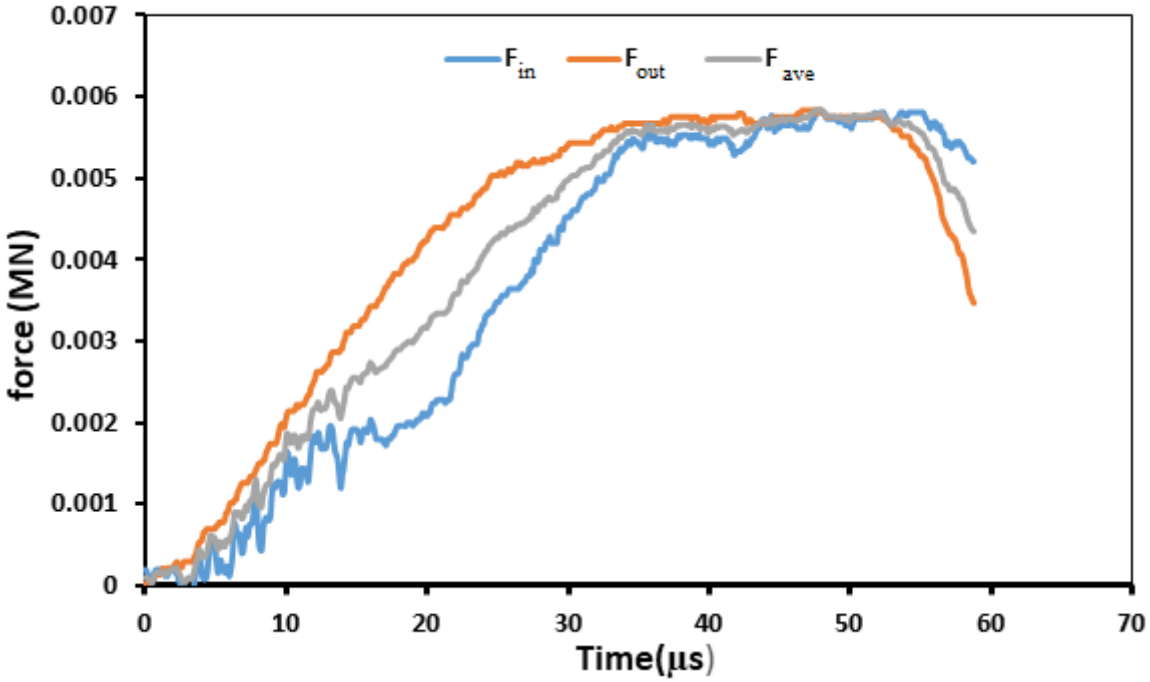

Figure 6. Forces in the two sides of the NSSS sample.

The displacements of the two sides of the sample are calculated based on Equations (5) and (6). U_{in}, U_{out}, and relative displacement U_{rel} of the two sides of the NSSS are shown in Figure 7. The samples with t_m = 1.5 mm and 2 mm were tested in the same strain rate to verify the effect of the geometry on the result of shear stress–strain curve (to achieve the same shear strain rate, the velocity of the striker bar was changed). Figure 8 shows the shear stress–strain curves of the sample with t_m = 1.5 mm and 2 mm at the same shear strain rate (to achieve the same shear strain rate for different geometry, the velocity of the impact is adjusted). The result shows that for both specimens, the shear strain rate is steady at a value of approximately 2000 s^{-1}, which shows that a constant shear strain rate can be

achieved under the dynamic compressive loading for the different geometry of NSSS. Moreover, the calculated shear stress–strain curves for both specimens agree well. The result indicates that the t_m does not have a considerable effect on the shear stress–strain curve and can thus be neglected. Hence, achieving a wide range of strain rate by the presented specimen is possible through changing the t_m and the impact velocity.

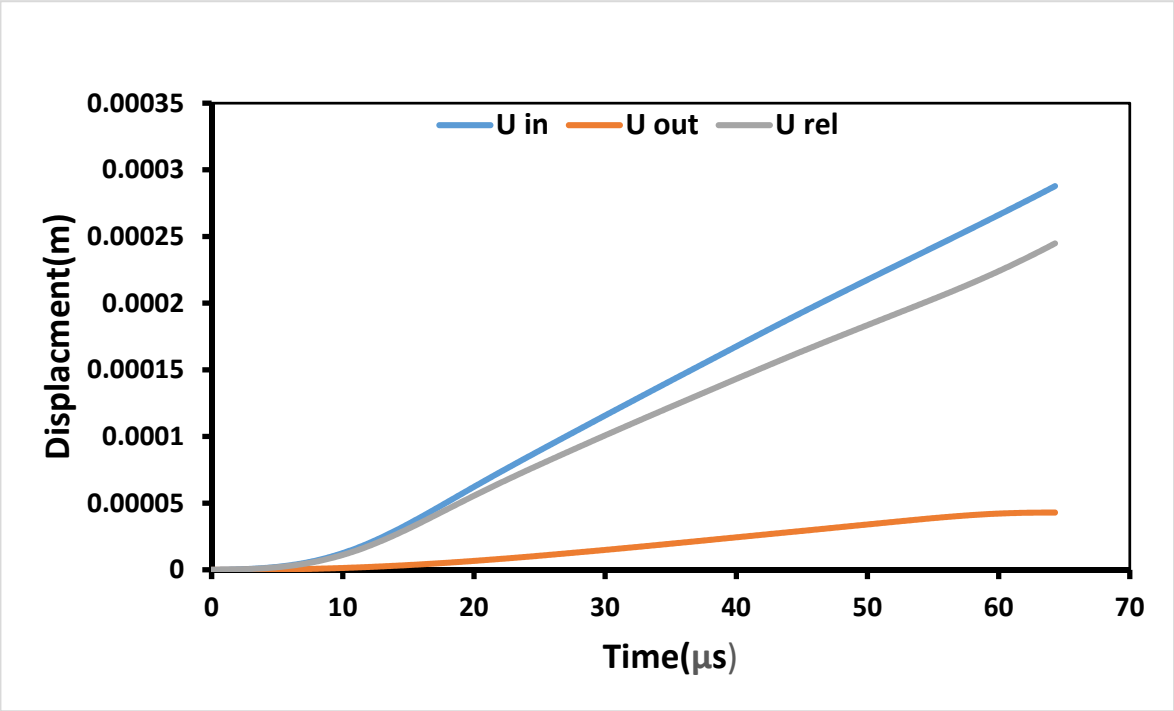

Figure 7. Displacements of the two sides of the NSSS.

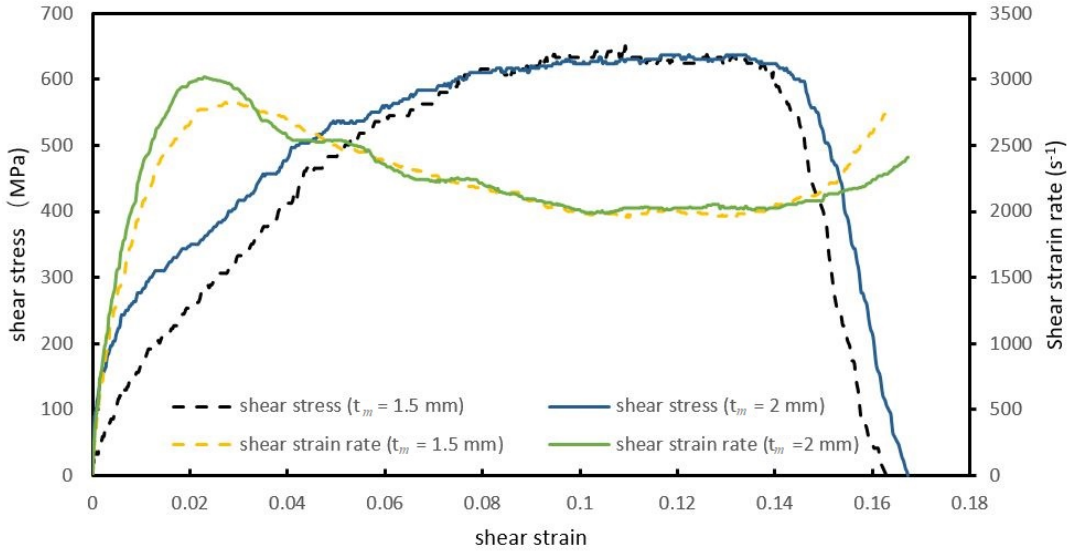

Figure 8. Shear stress–strain curves of the two geometries under the same strain rate.

Three tests were conducted under the same shear strain rate (the same geometry and same impact velocity) to check the repeatability of the experiment. To achieve the same strain rate, the impact velocity of the striker bar was kept constant. Figure 9 shows the results of these three tests. The results indicate that the shear stress–strain curves are repeatable.

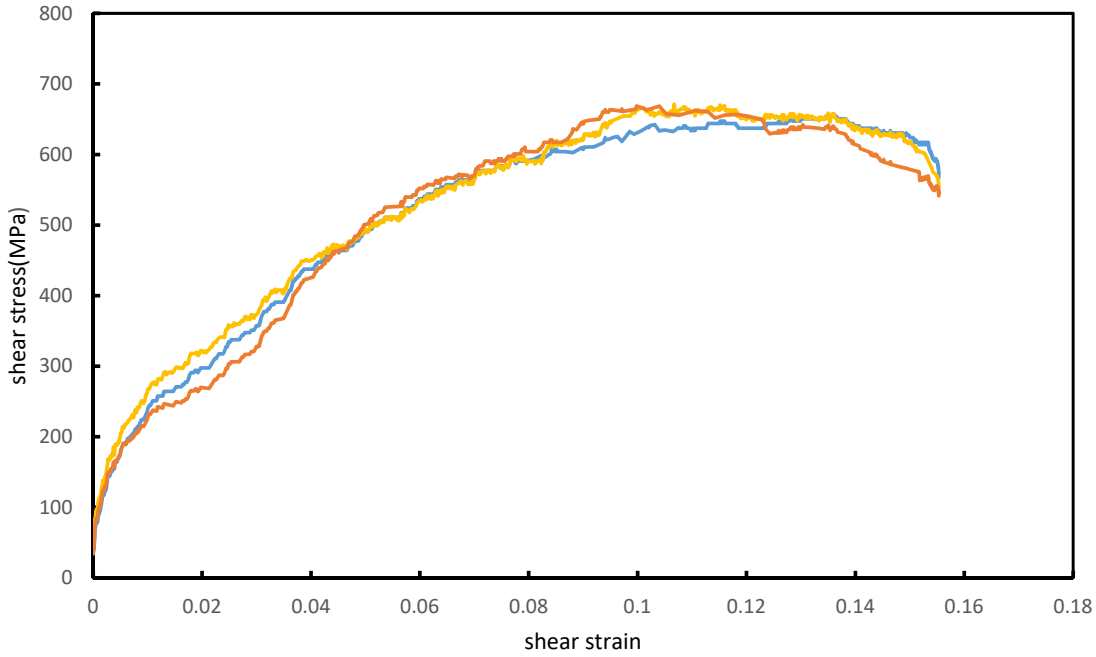

Figure 9. Three shear stress–strain curves of the NSSS under the same strain rate (900 s^{-1}).

Figure 10 shows the shear stress–strain curves of the Ti6Al4V measured by the new shear sample under various shear strain rates. The shear stress increases with the strain rate. In all strain rates, the flow stress increases slightly with the shear strain. This finding is in good agreement with the result of other researchers [1,20,30]. Peries et al. [20] tested the dynamic behavior of the Ti6Al4V by different geometry of the hat shape sample. They mentioned, because of the complex stress distribution in the hat shape sample, interpretation of the test results is not straight forward. The important differences between the shear stress–strain curve of the Ti6Al4V under the dynamic and the quasi-static experiment (in the strain rate of 0.1 s^{-1}) are observed. The shear stress under the quasi-static loading is much lower than the dynamic condition.

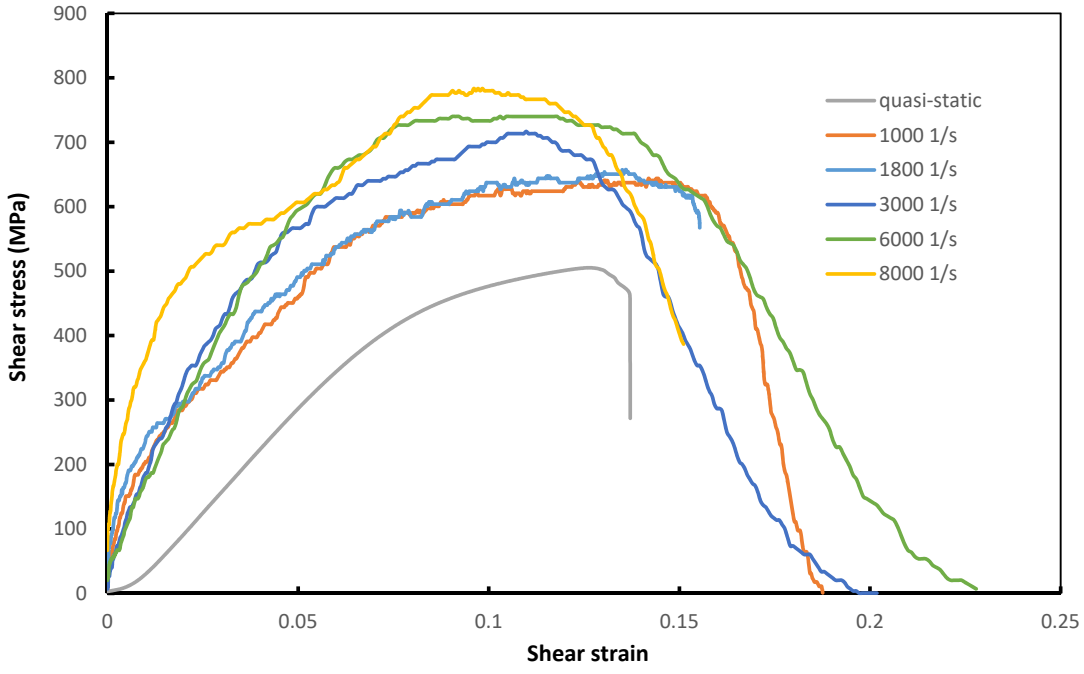

Figure 10. Shear stress–strain curves of Ti6Al4V with NSSS under different strain rates.

Figure 11 shows the failure of the NSSS under the quasi-static (Figure 11a) and dynamic loadings at strain rates of 1800 s^{-1} (Figure 11b) and 6000 s^{-1} (Figure 11c). The failure occurs in the shear zone. For the specimen under the dynamic condition, the failure shows pure shear failure; however, the failure under quasi-static loading is not pure shear. The width of the shear zone was measured by the DIC method, which will be discussed in the next section.

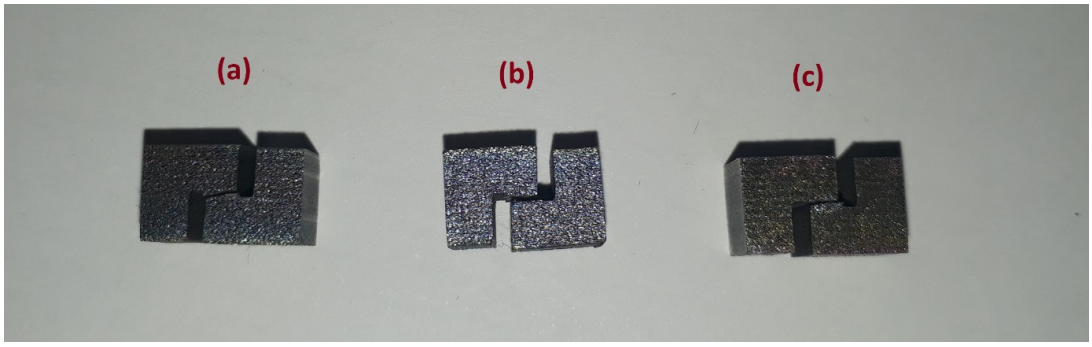

Figure 11. Failure of the NSSS sample under (**a**) quasi-static loading with strain rates of (**b**) 900 s^{-1} and (**c**) 3000 s^{-1}.

During the quasi-static experiment, sufficient time is available for the heat to be conducted away from the shear region, which prevents thermal softening and the formation of adiabatic shear. Osovski et al. [31] did not observe dynamic recrystallization under the quasi-static loading for Ti6Al4V specimen either; however, they observed that on a strain rate higher than 1000 s^{-1} dynamic recrystallization occurred for all specimens. They found that the deformation energy under quasi-static loading is higher than the dynamic condition, and quasi-static deformation is an isothermal phenomenon, whereas dynamic deformation is an adiabatic phenomenon. This explanation justifies the different behaviors of the Ti6Al4V specimen under the quasi-static loading compared with that under dynamic loading [20].

Figure 12 shows the fracture surface of the NSSS under the dynamic and quasi-static (0.001 s^{-1}) loadings. In quasi-static and dynamic loadings, smooth surface and dimple area coexisted. However, on the quasi-static loading, the area of the smooth surface is limited, implying different fracture mechanisms under the dynamic and quasi-static loadings. Smooth surface is mainly caused by rubbing between the fracture surface and the fragment [32,33]. Dimples are formed due to elongation along the maximum shear stress direction, which indicates the occurrence of a large plastic deformation. The average size of the dimples under quasi-static loading is bigger than that under dynamic condition. Similar observation was reported by Ran et al. [13], in which they reported that the size and depth of the dimples decrease with increasing strain rate.

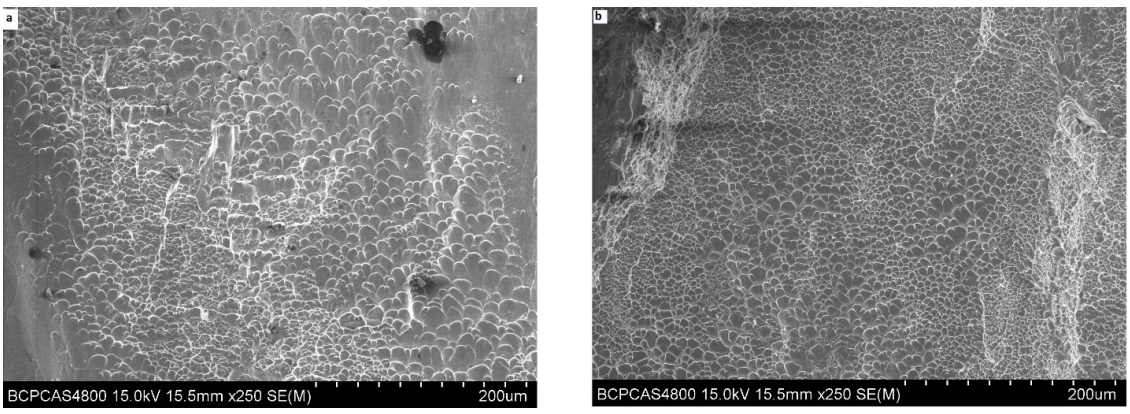

Figure 12. SEM images of the fracture surfaces of the NSSS. (**a**) Quasi-static loading and (**b**) dynamic loading (2500 s^{-1}).

3.2. DIC

The displacement field history can be measured by the DIC method. All the sample surfaces were selected as area of interest for the DIC method [34,35]. Figure 13 shows the evolution of the maximum principal strain field of the samples during the SHPB test. The figure shows nine frames during the test. Figure 13a shows the strain field when the stress wave arrives the surface of the specimen and incident bar. Figure 13b–j show the strain fields at 6.6, 13.2, 19.8, 26.4, 33, 39.6, 46.2, and 52.8 μs after load initiation, respectively. The maximum main strain occurs in the shear zone in the middle of the specimen. However, when failure occurs, measuring the displacement near the failure area is impossible because of the high deformation and vanished speckles. The trend of strain development can be obtained through the variations of the images. The DIC analysis indicates that at the 6.6 μs, the maximum shear strain is approximately the same in the whole area of the NSSS. However, in the corner of the NSSS, the maximum is slightly higher. Notably, after approximately 46 μs, the shear zone is completely formed in the middle of the sample (Figure 13f,g), and in the remaining part of the specimen, the maximum shear stress exhibits the same value. This finding indicates that pure shear loading occurs for the NSSS during the test. Ran et al. [24] found that in the flat hat-shaped sample the shear strain distribution was not equal.

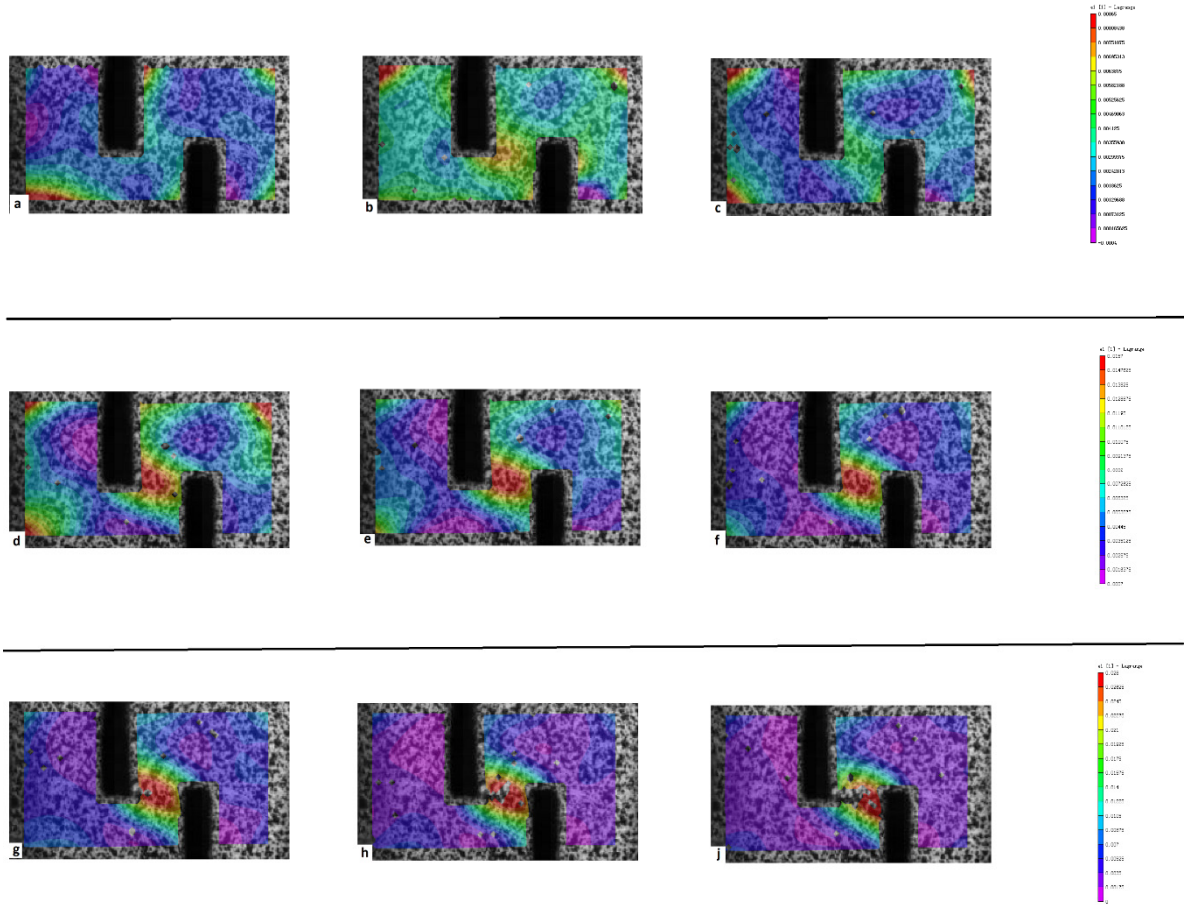

Figure 13. Maximum shear strain fields of the NSSS at different times during dynamic loading (**a**) 0 μs, (**b**) 6.6 μs, (**c**) 13.2 μs, (**d**) 19.8 μs, (**e**) 26.4 μs, (**f**) 33 μs, (**g**) 39.6 μs, (**h**) 46.2 μs, and (**j**) 52.8 μs.

As shown in Figure 14, a line is drawn in the center of the NSSS to study the shear strain in the shear zone and calculate the width of the shear zone in the NSSS. Figure 14 shows the distribution of shear strain on the line at different loading times. The strain value is not available at the times later than 40 μs because of the start of cracking. The values of shear strain increase with time at the same location of the shear zone. The result shows that the maximum shear strain occurs in the

center of the specimen, and by going from the edge of specimen, the shear strain value decreases. The symmetrical shape of the curve implies that the NSSS sample is insensitive to the direction of loading. Figure 14 indicates that the shear zone of the sample is localized in the center of the specimen with a thickness of approximately 2 mm. However, this shear width value is higher than that of the design (W_s = 0.2 mm). In most of the shear specimens, such as the hat-shaped and flat-hat-shaped, the plastic zone is considerably higher than expected, which leads to overestimation of the value of the reported strain calculated by Meyers methods [24].

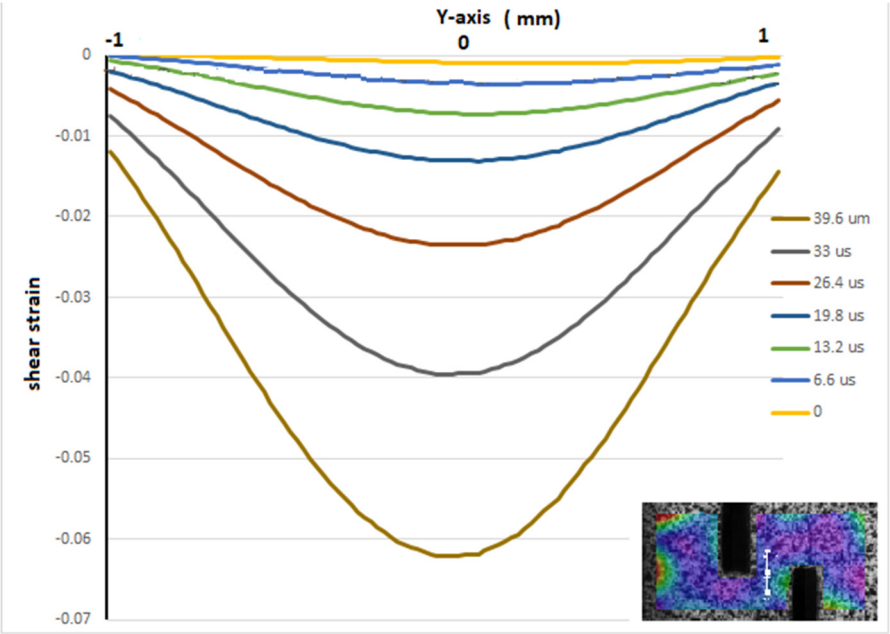

Figure 14. Distribution of shear stress on the Y-axis at different times.

3.3. FEM Simulation

Figure 15 shows the contour of the equivalent stress on the NSSS surface. These results show that the distributions of shear stress, shear strain, and Mises stress are uniform in the NSSS. The shear zone forms completely in the center of NSSS. As shown in Figures 13 and 15, the FEM result indicates good agreement with the DIC result. Figure 16 shows the comparison of strain signals in the incident and transmitted bars between the experiment and the simulation. Before 55 μs, the agreement between the experiment and the simulation is well, but after this point, the sample is broken in the test, and the stress pulse in the sample will all be reflected back into the incident bar, causing that the reflection signal in the incident bar is enhanced. Hence, the transmitted strain signal measured in the experiment has a shorter duration than the FEM simulation result.

Figure 17 shows the contour of equivalent stress on the shear gauge of NSSS. Simulation shows, after 6.6 μs, the stress distribution in all of the shear gauge area is found to be uniform, and the stress and strain measured with DIC method in the surface can present the value of the stress and strain in the whole shear gauge section.

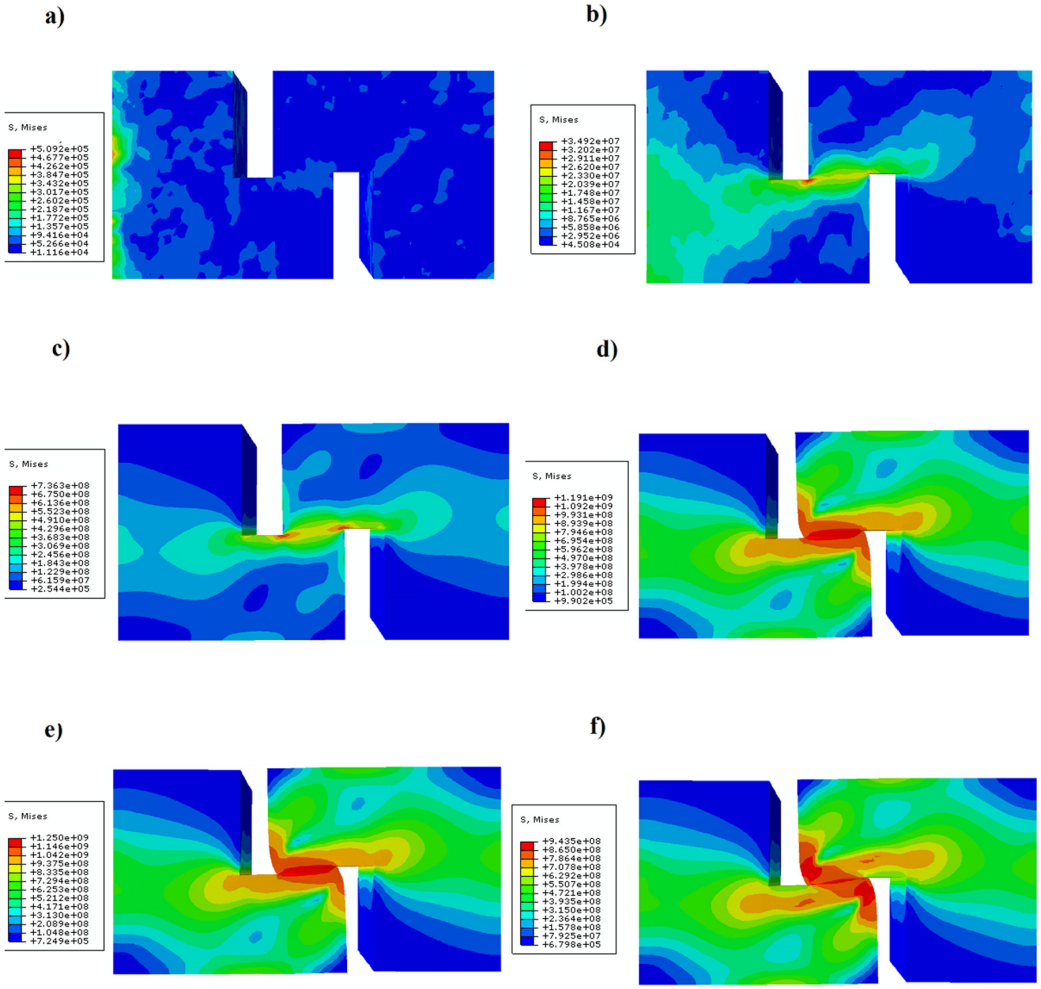

Figure 15. Contour of the equivalent stress on the NSSS surface (**a**) 0 μs, (**b**) 6.6 μs, (**c**) 30 μs, (**d**) 60 μs, (**e**) 90 μs, and (**f**) 110 μs.

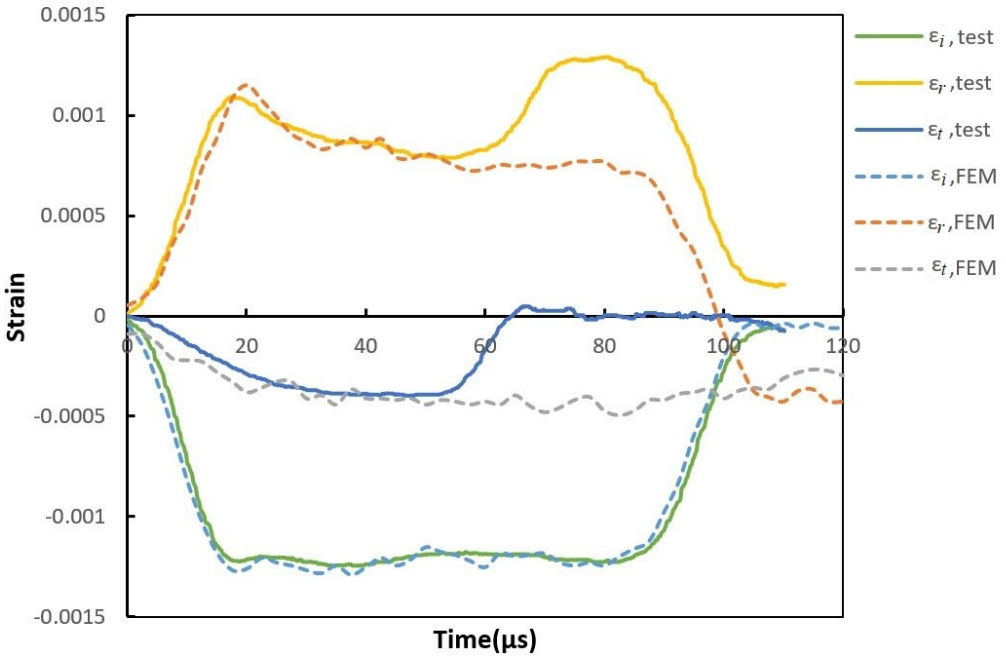

Figure 16. Comparison of strain signals in the incident and transmitted bars between the experiment and the simulation.

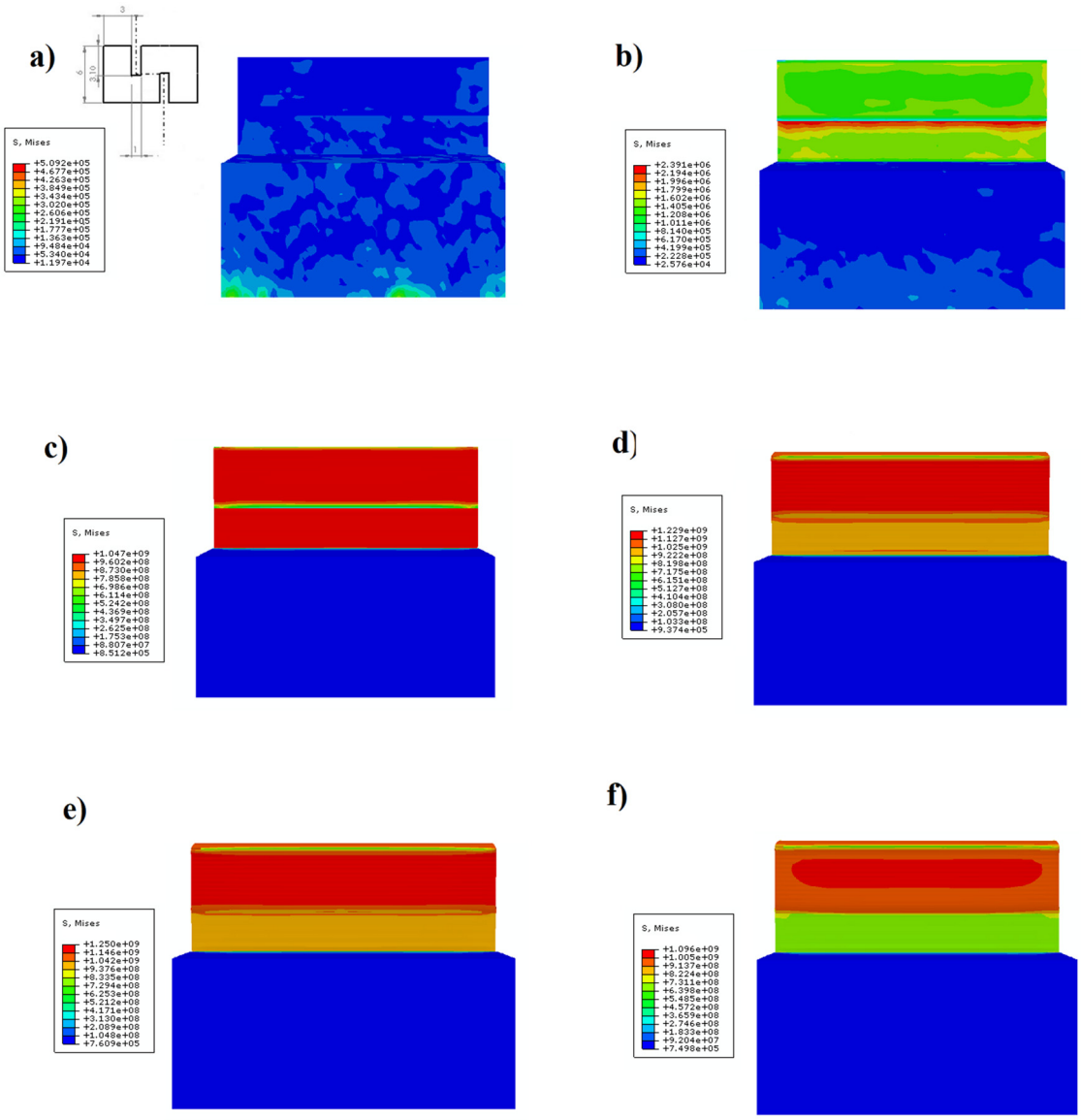

Figure 17. Contour of the equivalent stress on the shear gauge of NSSS (**a**) 0 μs, (**b**) 6.6 μs, (**c**) 30 μs, (**d**) 60 μs, (**e**) 90 μs, and (**f**) 110 μs.

Figure 18 shows the comparison of the displacements of the two sides of the NSSS obtained by simulation, DIC, and SHPB test. The simulation result indicates good agreement with experimental and DIC data. However, the DIC result shows larger displacement for the surface of the sample and incident bar at the beginning of loading. Comparison of the results indicate that the DIC method obtains a higher value of displacement in the early stage of impact, which results in a higher strain value. Calculating the shear strain based on the DIC method can cause calculation errors. However, the DIC error can be reduced by using a high-speed camera with a higher resolution. Figure 19 shows the shear stress–strain curves of the specimen obtained through experiment and FEM simulation. The results indicate that the shear stress–strain curves obtained through the experiment is in good agreement with the FEM simulation result until the NSSS fails and its shear stress drops. However in the elastic part of shear stress–strain curve, the result of FEM simulation is higher than the experimental result, which might be due to the parameters of J–C model.

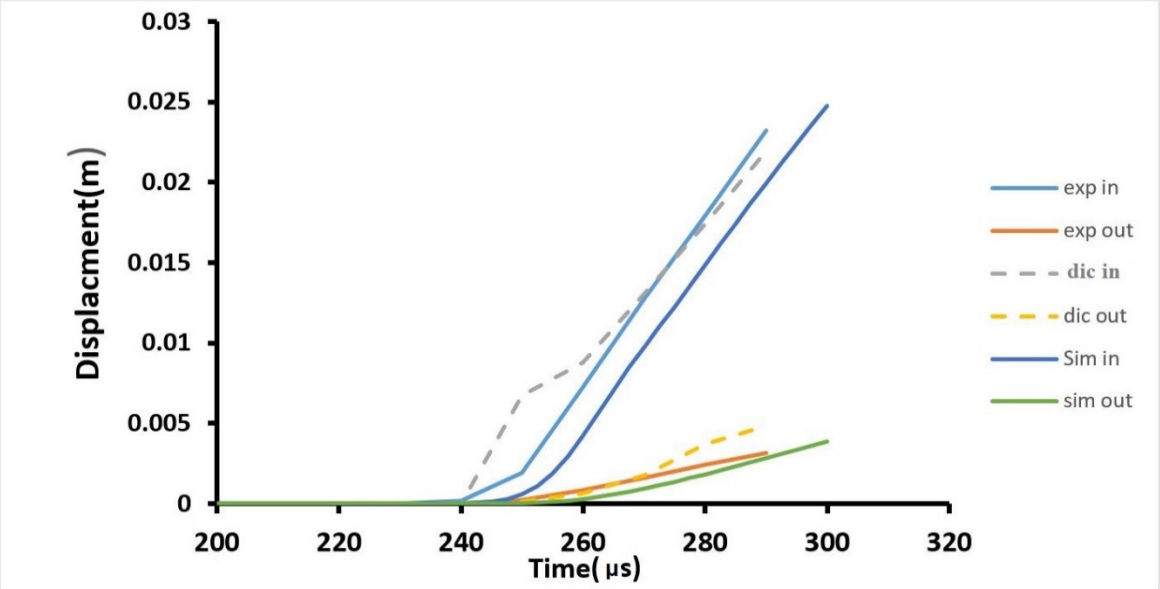

Figure 18. Displacement of two sides of the NSSS obtained by digital image correlation (DIC), simulation and SHPB.

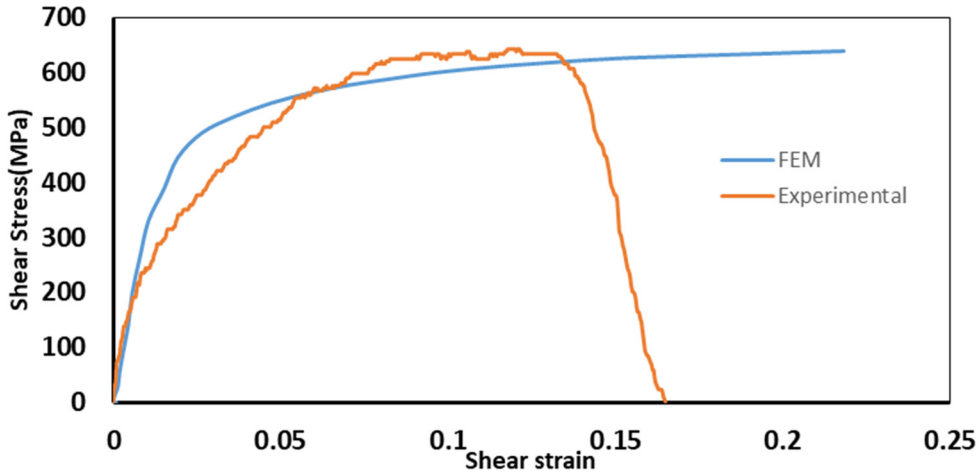

Figure 19. Shear stress–strain curve of the NSSS (t_m = 1.5 mm) under a strain rate of 1000 s^{-1}.

4. Conclusions

A newly designed S-shaped specimen was developed to study the dynamic shear behavior of materials. New specimens were tested under the static and dynamic loading by SHPB. DIC method and FEM simulation were used to validate the NSSS. NSSS can use conventional SHPB without any modification. Compared to the previous geometries for studying the dynamic shear band, the proposed geometry can achieve the force equilibrium in its two sides of the NSSS, and stress–strain curve can be directly measured. By changing t_m, the wide range of shear strain rate can be achieved. The simple geometry of the NSSS resulted in the formation of pure shear in the shear zone of sample under dynamic loading. Given the flat surface, the experiment can be easily coupled with the 2D-DIC method, which provides the full-field strain distribution. The dynamic shear behavior of Ti6Al4V was tested by this new specimen, and the results are in good agreement with those of previous studies. The result of this paper shows the NSSS can be used to study the dynamic shear behavior of various materials.

Author Contributions: A.A. designed the sample and study. A.A., Q.Z. and Y.G. carried out the dynamic tests and helped design the material tests. They contributed to sample preparation and they did the experiments and simulation. P.C. supervised the research. All authors discussed the results and contributed to the final manuscript.

Funding: This research was funded by National Natural Science Foundation of China, grant number 11472054.

Conflicts of Interest: The authors declare no conflict of interest.

References

1. Peirs, J.; Verleysen, P.; Degrieck, J. Novel technique for static and dynamic shear testing of Ti6Al4V sheet. *Exp. Mech.* **2012**, *52*, 729–741. [CrossRef]
2. Arab, A.; Chen, P.; Guo, Y. Effects of microstructure on the dynamic properties of TA15 titanium alloy. *Mech. Mater.* **2019**, *137*, 103121.
3. Rittel, D.; Wang, Z.G.; Dorogoy, A. Geometrical imperfection and adiabatic shear banding. *Int. J. Impact Eng.* **2008**, *35*, 1280–1292. [CrossRef]
4. Lins, J.F.C.; Sandim, H.R.Z.; Kestenbach, H.-J.; Raabe, D.; Vecchio, K.S. A microstructural investigation of adiabatic shear bands in an interstitial free steel. *Mater. Sci. Eng. A* **2007**, *457*, 205–218. [CrossRef]
5. Zheng, C.; Wang, F.; Cheng, X.; Liu, J.; Liu, T.; Zhu, Z.; Yang, K.; Peng, M.; Jin, D. Capturing of the propagating processes of adiabatic shear band in Ti-6Al-4V alloys under dynamic compression. *Mater. Sci. Eng. A* **2016**, *658*, 60–67. [CrossRef]
6. Zurek, A.K. The study of adiabatic shear band instability in a pearlitic 4340 steel using a dynamic punch test. *Metall. Mater. Trans. A* **1994**, *25*, 2483–2489. [CrossRef]
7. Wang, B.F.; Yang, Y. Microstructure evolution in adiabatic shear band in fine-grain-sized Ti-3Al-5Mo-4.5V alloy. *Mater. Sci. Eng. A* **2008**, *473*, 306–311. [CrossRef]
8. Wang, B.; Wang, X.; Li, Z.; Ma, R.; Zhao, S.; Xie, F.; Zhang, X. Shear localization and microstructure in coarse grained beta titanium alloy. *Mater. Sci. Eng. A* **2016**, *652*, 287–295. [CrossRef]
9. Odeshi, A.G.; Bassim, M.N.; Al-Ameeri, S. Effect of heat treatment on adiabatic shear bands in a high-strength low alloy steel. *Mater. Sci. Eng. A* **2006**, *419*, 69–75. [CrossRef]
10. Klepaczko, J.R. An experimental technique for shear testing at high and very high strain rates. The case of a mild steel. *Int. J. Impact Eng.* **1994**, *15*, 25–39. [CrossRef]
11. Xu, Z.; Ding, X.; Zhang, W.; Huang, F. A novel method in dynamic shear testing of bulk materials using the traditional SHPB technique. *Int. J. Impact Eng.* **2017**, *101*, 90–104. [CrossRef]
12. Lindholm, U.S.; Johnson, G.R. Strain-rate effects in metals at large shear strains. In *Material Behavior Under High Stress and Ultrahigh Loading Rates, Mescall, J.*; Weiss, W., Ed.; Springer: Boston, MA, USA, 1983; pp. 61–79.
13. Ran, C.; Chen, P.; Li, L.; Zhang, W.; Liu, Y.; Zhang, X. High-strain-rate plastic deformation and fracture behaviour of Ti-5Al-5Mo-5V-1Cr-1Fe titanium alloy at room temperature. *Mech. Mater.* **2018**, *116*, 3–10. [CrossRef]
14. Ran, C.; Chen, P.; Li, L.; Zhang, W. Dynamic shear deformation and failure of Ti-5Al-5Mo-5V-1Cr-1Fe titanium alloy. *Mater. Sci. Eng. A* **2017**, *694*, 41–47. [CrossRef]
15. Rittel, D.; Lee, S.; Ravichandran, G. A shear-compression specimen for large strain testing. *Exp. Mech.* **2002**, *42*, 58–64. [CrossRef]
16. Dorogoy, A.; Rittel, D. Numerical validation of the shear compression specimen. Part I: quasi-static large strain testing. *Exp. Mech.* **2005**, *45*, 167–177. [CrossRef]
17. Dorogoy, A.; Rittle, D. Numerical validation of the shear testing, specimen. Part II: dynamic large strain. *Exp. Mech.* **2005**, *45*, 178–185. [CrossRef]
18. Guo, Y.; Li, Y. A novel approach to testing the dynamic shear response of Ti-6Al-4V. *Acta Mech. Solida Sin.* **2012**, *25*, 299–311. [CrossRef]
19. Gray, G.T.; Vecchio, K.S.; Livescu, V. Compact forced simple-shear sample for studying shear localization in materials. *Acta Mater.* **2016**, *103*, 12–22. [CrossRef]
20. Peirs, J.; Verleysen, P.; Degrieck, J.; Coghe, F. The use of hat-shaped specimens to study the high strain rate shear behaviour of Ti-6Al-4V. *Int. J. Impact Eng.* **2010**, *37*, 703–714. [CrossRef]
21. Jiang, Y.; Chen, Z.; Zhan, C.; Chen, T.; Wang, R.; Liu, C. Adiabatic shear localization in pure titanium deformed by dynamic loading: Microstructure and microtexture characteristic. *Mater. Sci. Eng. A* **2015**, *640*, 436–442. [CrossRef]
22. Ma, Y.; Yuan, F.; Yang, M.; Jiang, P.; Ma, E.; Wu, X. Dynamic shear deformation of a CrCoNi medium-entropy alloy with heterogeneous grain structures. *Acta Mater.* **2018**, *148*, 407–418. [CrossRef]

23. Meyer, L.W.; Halle, T. Shear strength and shear failure, overview of testing and behavior of ductile metals. *Mech. Time-Dependent Mater.* **2011**, *15*, 327–340. [CrossRef]
24. Ran, C.; Chen, P. Dynamic shear deformation and failure of Ti-6Al-4V and Ti-5Al-5Mo-5V-1Cr-1Fe alloys. *Materials* **2018**, *11*, 76. [CrossRef]
25. Sutton, M.A.; Orteu, J.-J.; Schreier, H.W. *Image Correlation for Shape, Motion and Deformation Measurements: Basic Concepts, Theory and Applications*; Springer Science & Business Media: New York, NY, USA, 2009.
26. Huimin, P.B.X. Full-field strain measurement based on least-square fitting of local displacement for digital image correlation method. *Acta Opt. Sin.* **2007**, *11*, 014.
27. Dorogoy, A.; Rittel, D. Determination of the johnson-cook material parameters using the SCS specimen. *Exp. Mech.* **2009**, *49*, 881–885. [CrossRef]
28. Wang, B.; Liu, Z. Shear localization sensitivity analysis for Johnson-Cook constitutive parameters on serrated chips in high speed machining of Ti6Al4V. *Simul. Model. Pract. Theory* **2015**, *55*, 63–76. [CrossRef]
29. Gama, B.A.; Lopatnikov, S.L.; Gillespie, J.W. Hopkinson bar experimental technique: A critical review. *Appl. Mech. Rev.* **2004**, *57*, 223. [CrossRef]
30. Verleysen, P.; Peirs, J. Quasi-static and high strain rate fracture behaviour of Ti6Al4V. *Int. J. Impact Eng.* **2016**, *000*, 1–19. [CrossRef]
31. Osovski, S.; Nahmany, Y.; Rittel, D.; Landau, P.; Venkert, A. On the dynamic character of localized failure. *Scr. Mater.* **2012**, *67*, 693–695. [CrossRef]
32. Rittel, D.; Wang, Z.G. Thermo-mechanical aspects of adiabatic shear failure of AM50 and Ti6Al4V alloys. *Mech. Mater.* **2008**, *40*, 629–635. [CrossRef]
33. Zhang, J.; Tan, C.-W.; Ren, Y.; Yu, X.-D.; Ma, H.-L.; Wang, F.-C.; Cai, H.-N. Adiabatic shear fracture in Ti-6Al-4V alloy. *Trans. Nonferrous Met. Soc. China* **2011**, *21*, 2396–2401. [CrossRef]
34. Tiwari, V.; Sutton, M.A.; Shultis, G.; McNeill, S.R.; Xu, S.; Deng, X.; Fourney, W.L.; Bretall, D. Measuring full-field transient plate deformation using high speed imaging systems and 3D DIC. *Soc. Exp. Mech. SEM Annu. Conf. Expo. Exp. Appl. Mech.* **2009**, *1*, 481–488.
35. Gao, G.; Huang, S.; Xia, K.; Li, Z. Application of digital image correlation (DIC) in dynamic notched semi-circular bend (NSCB) tests. *Exp. Mech.* **2015**, *55*, 95–104. [CrossRef]

© 2019 by the authors. Licensee MDPI, Basel, Switzerland. This article is an open access article distributed under the terms and conditions of the Creative Commons Attribution (CC BY) license (http://creativecommons.org/licenses/by/4.0/).